International Journal of Heat and Mass Transfer 255 (2026) 127880

Contents lists available at ScienceDirect

International Journal of Heat and Mass Transfer

journal homepage: www.elsevier.com/locate/ijhmt

Experimental investigation on droplet size in post-dryout region

Zihan Xia *, Nikolai Rensch, Xu Cheng

Institute for Applied Thermofluidics (IATF), Karlsruhe Institute of Technology (KIT), Kaiserstrasse 12, 76131, Karlsruhe, Germany

ARTICLE INFO

Keywords:
Visualized droplet experiment
Droplet size
Post-dryout (PDO)
Dispersed flow

ABSTRACT

Due to the limited availability of experimental data on droplet size in dispersed flow under post-dryout (PDO) conditions, and its critical role in accurately predicting PDO heat transfer, this study designs and conducts a visualization experiment to investigate droplet behavior in PDO regime. A square flow channel with a centrally positioned electrically heated tube is constructed, installing multiple observation windows on both side walls to provide optical access to the droplets. Experiments are conducted under heat fluxes exceeding the critical heat flux (CHF), ensuring the observation area within the PDO regime. Droplet motion in the vapor flow is recorded by the high-speed camera through transparent windows. The droplet size and their distributions are extracted and analyzed under various operating conditions. The obtained data are combined with literature datasets to evaluate existing droplet size correlations. The results show that current droplet size correlations do not accurately predict the data. Therefore, a new droplet size correlation based on the droplet Weber number is developed, demonstrating good predictive performance over a range of operating conditions.

1. Introduction

In heat exchange systems, dryout can lead to a sharp increase in the wall temperature of heated surfaces. The heat transfer performance in the post-dryout (PDO) region is critical in determining the maximum surface temperature, which is of key importance for the thermal design and safety analysis of heat exchange systems. In the PDO region, the flow regime is figured out as dispersed flow. The heated wall is no longer wetted by liquid and transfers heat directly to the vapor phase. The vapor is thus superheated and transfer heat to droplet driven by the thermal non-equilibrium. However, the complex dynamics of droplets in the dispersed flow make it difficult to quantify the degree of thermal non-equilibrium and actual vapor temperature, which in turn limits the prediction accuracy of the maximum wall temperature of heated surface. Therefore, improved modeling of PDO heat transfer are essential to determine whether the structural integrity of heated surfaces can be maintained under various operating and accident conditions.

Several methods are commonly employed to predict the PDO heat transfer, including empirical correlations [1,2], mechanistic models [3,4], and computational fluid dynamics (CFD) simulations [5–8]. Empirical correlations are typically developed by fitting experimental data but often have limited applicability beyond the database which they were derived. In contrast, mechanistic models aim to describe the individual processes-such as wall-vapor convection heat transfer and vapor-droplet interfacial heat transfer in the PDO region, offering stronger physical meanings and broader applicability. However, parameters such as droplet size, droplet velocity, and void fraction exhibit complex multi-dimensional distributions that are difficult to capture in one-dimensional models. With the advancement of computational science, CFD has been increasingly employed to simulate PDO heat transfer. By solving sets of two-dimensional or three-dimensional governing equations numerically, the trajectories of droplets and their interactions with the wall and vapor flow can be simulated in detail, enabling a more comprehensive understanding of the underlying physical processes. It should be noted that in numerical models, the heat transfer coefficients between droplets and vapor, as well as the collision models between droplets and the wall, still rely on empirical correlations like those used in mechanistic models.

From the investigation on the heat transfer of droplets in superheated vapor [9,10], the basic format for describing the droplets evaporation in superheated vapor is:

$$Q_{vd} = h_{vd}\Delta T n_d \pi d^2 = \frac{Nu_{vd}k_v}{d}\Delta T \frac{6(1-\alpha)}{d} A_f \Delta z \tag{1}$$

$$Nu_{vd} = \frac{h_{vd}d}{k_v} = 2.0 + C_1 Pr_v^a Re_d^b \tag{2}$$

In Equations (1), the interfacial heat transfer power is calculated by the multiplication of interfacial heat transfer coefficient h_{vd}, thermal

* Corresponding author.
E-mail address: zihan.xia@kit.edu (Z. Xia).

https://doi.org/10.1016/j.ijheatmasstransfer.2025.127880
Received 23 July 2025; Received in revised form 12 September 2025; Accepted 23 September 2025
Available online 27 September 2025

Nomenclature

a	exponent
A_f	Flow area (m^2)
b	exponent
C_1	constant
C_D	Drag coefficient
d	Droplet diameter (m)
d_{10}	arithmetic mean droplet diameter (m)
d_{do}	droplet diameter at dryout point (m)
D_t	Tube diameter (m)
Δu	Interfacial velocity difference (m/s)
ΔT	Temperature difference between vapor and droplet (K)
Δz	Length of control volume (m)
G	Mass flux, (kg/ m^2·s)
h_{vd}	Interfacial heat transfer coefficient (w/ m^2·K)
h_{lg}	Latent heat (J/kg)
k	Thermal conductivity (W/m-K)
n_d	Droplet number
Nu	Nusselt number
P	Pressure, bar
Pr	Prandtl number
P_R	Reduced pressure
Q	Heat power (W)
q''	Heat flux (W/m^2)
Re_d	Droplet Reynolds number
Re_v	Vapor Reynolds number
T_{in}	Inlet fluid temperature (°C)
u_g	Average gas phase velocity in axial direction (m/s)
u_v	Average vapor velocity in axial direction (m/s)
We_{cr}	Critical Weber number
We_d	Droplet Weber number
x_e	Equilibrium steam quality
x_a	Actual steam quality

Greek symbols

α	Void fraction
μ	Dynamic viscosity (Pa-s)
ρ	Density (kg/m^3)
σ	Surface tension (N/m)

non-equilibrium degree ΔT and droplet surface area $n_d\pi d^2$. The droplet size is key importance for the interfacial heat transfer. The impact of droplet size on interfacial heat transfer can be summarized in two aspects: 1) heat transfer area: a reduction of droplet diameter by a factor of two leads to approximately a fourfold increase in the total interfacial area at the same steam quality, thereby enhancing heat transfer; 2) interfacial heat transfer coefficient: Droplet size also affects the interfacial Nusselt number Nu_{vd} by modifying the relative Reynolds number Re_d. Larger droplets generally induce higher relative velocities, resulting in larger Reynolds numbers and hence higher Nusselt numbers, which enhances interfacial heat transfer efficiency. From our previous CFD simulation [7], smaller droplets tend to strengthen interfacial heat transfer, thereby lowering the wall temperature.

Besides, within the short distance after dryout, the wall temperature could still be low and droplets can wet the heated surface to have efficient heat removal. In this case, the droplet size is also important for predicting the amount of droplets reaching the wall and wall-droplet contact heat transfer [3,11].

During the prediction of PDO heat transfer in mechanistic models and CFD simulations, the droplet size at the dryout point should be known as part of the initial calculation procedure [12–14] and is considered important for the prediction accuracy of the PDO wall temperature [15,16]. For simplifying calculations, the average droplet size was often employed [17,18]. For example, Matsuura et al. [19] assumed a simplified average droplet size of 100 μm at the dryout point in their PDO model. In the actual conditions, the droplets are not in one uniform size but follows certain distributions in PDO region. Therefore, the study of droplet size is usually conducted together with the study of droplet distribution.

The droplet size correlations used in previous PDO heat transfer predictions can be categorized into two types: correlations from annular flow regime and correlations from dispersed flow regime. For correlations from annular flow, the research work posits that droplets are generated in the period of annular flow, suggesting that droplet size at dryout point should be derived from annular flow. For example, many research efforts are to analyze the droplet size based on the mechanism of droplet formulation and development history during the annular flow. Tatterson et al. [20] took the Kelvin-Helmhotlz instability mechanism as the primary mechanism during the droplet sizing process. When the vapor with high velocity flows through the agitated surface of liquid film with quite low velocity, the pressure at the wave crest is smaller than in the trough. The pressure difference acts as the suction force on the crest and torn the crest. The surface tension force of the torned crest resists the suction force until the pressure difference is larger enough to remove the part of liquids from the crest. The removed liquids are entrained into the main flow in the form of droplets. Based on this mechanism, they performed force balance analysis on the wave crest and derived the droplet size model for annular flow. The upper limit log-normal distribution is selected by Tatterson et al. [20] as the droplet distribution according to the work of Lopes and Dukler [21] and Evans et al. [22].

Yoder and Rohsenow [4] considered both the droplet formation mechanism and sizing during the development history. Several sizing sequences before the dryout point were analyzed. The Tatterson's correlation was selected for representing the sizing process due to Helmholtz instability. The maximum droplet size was determined according to the film slip Weber number, which was set as 6.5. By combining the three droplet sizing mechanisms, the droplet size correlation at the dryout point can be obtained by the cumulative mass distribution from the droplet generation position to the dryout point. Yoder's model was implemented in the PDO model of Yu [17] and Varone and Rohsenow [18].

In the work of Kataoka et al. [23], the type of roll wave shearing off was considered as the main droplet entrainment and sizing mechanism. The force balance equation between the interfacial drag force and surface tension force was established. Factors then were correlated with experimental data. This correlation is used in the model of Guo and Mishima [3].

Another method focusing on experimental investigation on droplet size on dryout and PDO region. For example, Ueda and Kim [24] conducted dryout experiments with R113 as working fluid. The mass flux ranged from approximately 200 to 900 kg/m^2·s at a constant pressure of 3.24 bar. The droplet size and distribution at the dryout point were obtained. From the experiment data it was found that the droplet size is smaller in higher vapor velocity. And the droplet size follows gamma distribution. After combined with data obtained by air-water system [25], a correlation for average droplet size was developed. The Ueda's data points were also used by Schnittger [26]. Schnittger included 30 experimental data points from literature and obtained a correlation for droplet mean diameter.

Besides, Cumo et al. [27] conducted a photographic experiment with Freon 12 as the working fluid. The reduced pressure ranged from 0.3 to 0.96, and the mass flux was maintained at approximately 900 kg/m^2·s. The experimental data of droplet size and distribution were obtained from the visual test section. The experimental data extracting from the

images showed that the average droplet size is smaller at high pressure conditions. The value of equilibrium steam quality is larger than 1 in most cases in Cumo's work, which means that the observing points mostly fallen in very dry PDO region. But the distance between the observing point and the dryout point is unknown from experimental data. A correlation for most probable droplet size in PDO region was developed based on droplet Reynold number and reduced pressure. Since a gamma distribution is concluded in Cumo's work, the average droplet size is considered 2 times of the most probable droplet size.

The existing correlations for droplet size are either derived from theoretical analysis without experimental validation or fitted from limited datasets, require obviously further assessment with additional experimental data.

Existing droplet measurement methods can be broadly divided into non-optical and optical techniques. Non-optical methods, such as drop collection [24,25] and conductance probes, are relatively simple to implement and applicable. However, they are intrusive in nature and typically provide only localized information, which limits their accuracy in representing the actual flow field. Optical techniques, by contrast, enable non-intrusive characterization of droplet size and velocity. Laser diffraction was widely adopted in earlier studies of droplet size in annular flow [28] due to its capability to provide rapid size distribution measurements. Nevertheless, it requires prior assumptions about the particle size distribution and becomes unreliable at high droplet concentrations because of multiple scattering effects. Phase Doppler anemometry (PDA) enables accurate, pointwise measurements of droplet size and velocity with high temporal resolution [29]. The technique requires careful scattering angle selection to ensure dominant light scattering modes, provides single-point rather than whole-field measurements, necessitates clear optical access for both transmitting and receiving optics, and exhibits inherent trade-offs between measurement range and resolution. Optical fiber probe (OFP) methods use micro-scale sensing tips to detect droplets based on refractive index differences, enabling simultaneous measurement of multiple droplet parameters [30]. Like PDA, OFP requires pointwise measurements with traversing mechanisms to map flow fields and requiring extensive installation work. High-speed imaging, on the other hand, allows direct visualization of droplet formation and dynamics over a wide field of view and is also a widely used droplets measurement technique [27,31]. Its limitations include finite spatial resolution and difficulty in detecting very small droplets. Given that high-speed imaging offers a straightforward experimental setup, does not disturb the flow or droplet dynamics, and provides direct visualization of droplet behavior in the PDO region, it is particularly suitable for the objectives of this work.

Consequently, this study performs droplet visualization experiments in the PDO region with high speed camera. The droplets are recorded through transparent window to investigate droplet dynamics under different operating conditions. Furthermore, the experimentally obtained droplet data are utilized to evaluate and improve existing droplet size correlations.

2. Experimental facility and measurement

The droplet visualization experiments are conducted in a square channel using R-134a as the working fluid. R-134a is selected as the working fluid due to its thermophysical similarity to water and relatively low critical pressure and latent heat. Transparent windows on the channel provide optical access for visualizing droplet behavior within the flow, aiming to capture and analyze droplet dynamics under PDO conditions, where direct observation is often challenging.

2.1. Experimental setup

2.1.1. Experimental loop

The experimental apparatus KIMOF was designed and constructed to study heat transfer behaviors in the PDO region [1]. The system is a closed-loop facility, as shown in Fig. 1, ensuring controlled experimental conditions. The major components of the experimental setup include pressurizer, main pump, preheater, electric flow heater, process valve, Coriolis flowmeter and test section. The pressurizer maintains the system pressure at the desired level, ensuring stable operating conditions. The main pump circulates the R-134a within the closed loop, where the fluid is initially heated by either the preheater or the electric flow heater to achieve the desired inlet temperature before entering the test section. The process valve allows fine control of the mass flow rate, measured by the Coriolis flowmeter before entering the test section and ensuring precise adjustment of experimental parameters. Within the test section, the fluid is further heated by the heating tube to reach dryout and PDO conditions.

2.1.2. Test section

As shown in Fig. 2, the test section is >3 m long and consists of 3 square flow channels with one heating tube in the center. Each square channel is around 1 m long. One piece of square channel contains 16 optical windows on parallel sides, enabling direct observation of the flow conditions inside the channel. The three square flow channels are connected with flanges, ensuring both a secure connection and precise alignment. The heating tube is positioned inside the square channel using 10 spacers to ensure proper alignment and to avoid contact between the heating tube and the inside channel wall. Fig. 3 displays the cross-sectional view of test section. The heating tube in the middle has an outer diameter of 10 mm, while the square channel has an inner width of 14 mm. The blue region in Fig. 3 is the flow area of the working fluid. To monitor the thermal conditions within the test section, in total 20 thermocouples are installed along the inner side of the heating tube at 12 levels, as shown with the orange circles in Fig. 3. The glass windows allow the high-speed camera to capture detailed droplet dynamics under PDO conditions.

The test section is heated using a direct current (DC) supplied by a transformer. The temperature and pressure of the fluid at both the inlet and outlet are measured using a mineral-insulated type-T thermocouple and a pressure transmitter, respectively. To ensure a fully developed flow at the beginning of the heated section, the distance between the tube entrance and the bottom current connector is set to approximately 430 mm. To minimize heat loss, the test section is insulated with two protective layers, maintaining stable thermal conditions within the test section.

A high-speed imaging system is utilized to capture droplet behavior

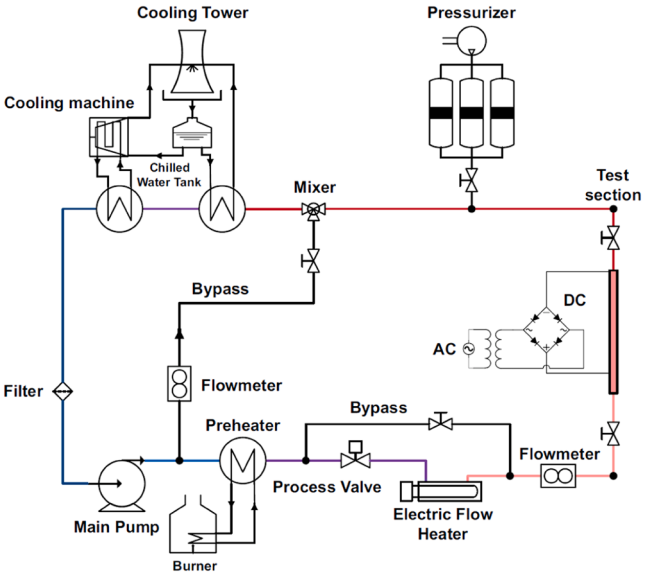

Fig. 1. Schematic set-up of the KIMOF [1].

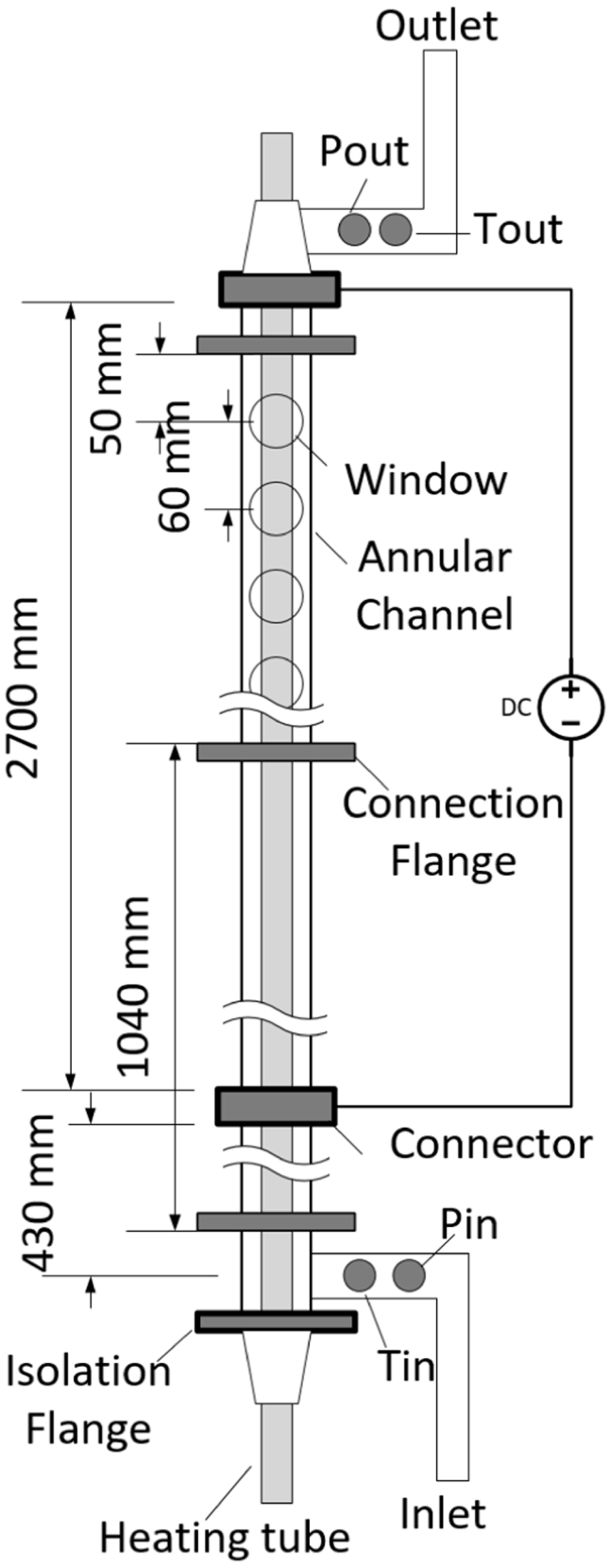

Fig. 2. Schematic of test section.

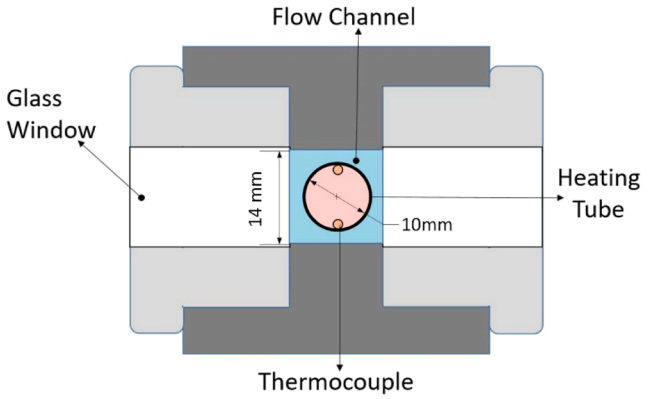

Fig. 3. Cross-sectional view of the test section.

with high temporal and spatial resolution. As shown in Fig. 4, the measurement setup comprises an LED backlight that provides uniform illumination through the transparent test section. The high-speed camera, positioned directly opposite the light source, recorded the droplets flowing inside the channel. Optronis high-speed video camera plus sigma macro lens are installed together to record the droplet behaviors. A glass plate is attached on the outer surface of window on the light side. The pane of glass is Plexiglas GS white WH010 with a thickness of 3 mm, which minimizes the effect of the individual LED light sources per panel through appropriate light refraction and have more uniform light going inside the channel and camera. The camera is focused on the center of the flow region. The diameter of the heating tube is used as a reference scale to measure the droplet size.

2.2. *Experimental matrix*

To investigate the effects of key thermal-hydraulic parameters on droplet behavior in the PDO region, a series of experiments are conducted under varying conditions of pressure, heat flux, inlet temperature, and mass flux. The experimental matrix is shown in Table 1. The selection of these test conditions allows for the evaluation of multiple influencing factors:

Pressure: The system pressure ranges from 16.2 bar to 32.5 bar, corresponding to a reduced pressure from 0.4 to 0.8. This range covers the typical operating pressure range encountered in several industrial heat exchangers. This broad pressure range allows for a comprehensive investigation of pressure effects on droplet behavior.

Heat Flux: The applied heat flux ranges from 20 kW/m^2 to 40 kW/m^2, enabling the investigation of effects of heat flux on droplet size. Within this range, a stable dispersed flow regime is established in the region of interest. If the heat flux is too low, excessive liquid presence can obstruct the optical window, while an overly high heat flux can lead to very high steam quality, causing droplets to become barely visible or completely evaporated.

Mass Flux: Two mass flux levels, 100 kg/(m^2·s) and 150 kg/(m^2·s),

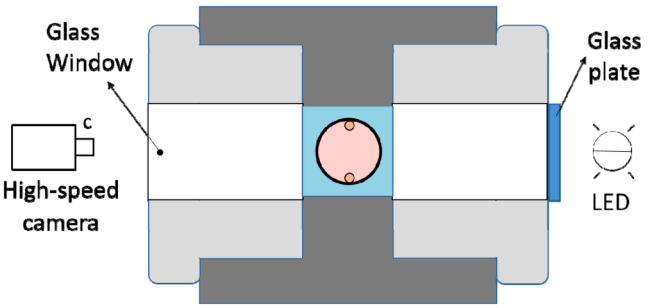

Fig. 4. Schematic of the arrangement of optical instruments.

Table 1
Experiment parameters.

Case number	Pressure (bar)	Heat flux (kW/m^2)	T_{in} (°C)	Mass Flux (kg/(m^2·s))
1	16.2	25	25.18	100
2	20.3	24	43.14	100
3	20.3	27	37.74	100
4	20.3	30	55.37	100
5	20.3	35	55.02	150
6	20.3	37.5	54.91	150
7	20.3	40	49.39	150
8	28.4	22.5	64.67	100
9	32.5	20	68.6	100

are selected to investigate the influence of mass flow rate on droplet behavior. Higher mass fluxes are avoided due to limitations of the test facility: excessive liquid volume fraction at higher flow rates tends to cover the observation window, making it difficult to visualize and track droplet motion within the channel.

2.3. Experimental operation

Each single PDO experiment is carried out at constant inlet temperature, mass flux and pressure as steady-state experiments. As the system parameters are stabilized to the desired mass flux, the heat power of the heating tube is gradually increased until the topmost thermocouple in the test section detects a sudden temperature jump, indicating the occurrence of dryout. Heat flux continues to be increased until the droplets in the topmost optical windows become clearly visible. Then the droplets inside the flow channel are recorded. This systematic approach ensures that droplet behaviors are captured under well-defined thermal-hydraulic conditions, providing high-quality experimental data for model validation and refinement.

Fig. 5 presents a sample of image acquired during the experiment. In this image, the central black region corresponds to the heating tube, while the grey areas on both sides represent the transparent windows through which the droplet behaviors inside the flow channel is visualized. The droplets appear as scattered dark spots within the illuminated region, where their size and motion are recorded into a sequence of images.

As observed in Fig. 5, the left part of the flow channel provides a clear view of the droplet distribution. Therefore, the left side under different heat flux are displayed together in Fig. 6 to show the trend of droplet size and number as the heat power increases. With same mass flux and pressure conditions, an increase in heating power results in fewer remaining droplets within the flow channel. Additionally, the size of the droplets decreases as the heating power increases.

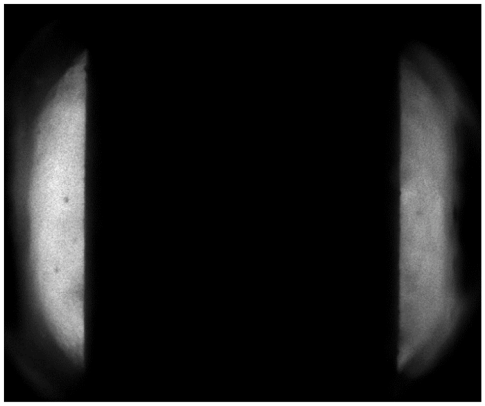

Fig. 5. Original image captured by high-speed camera.

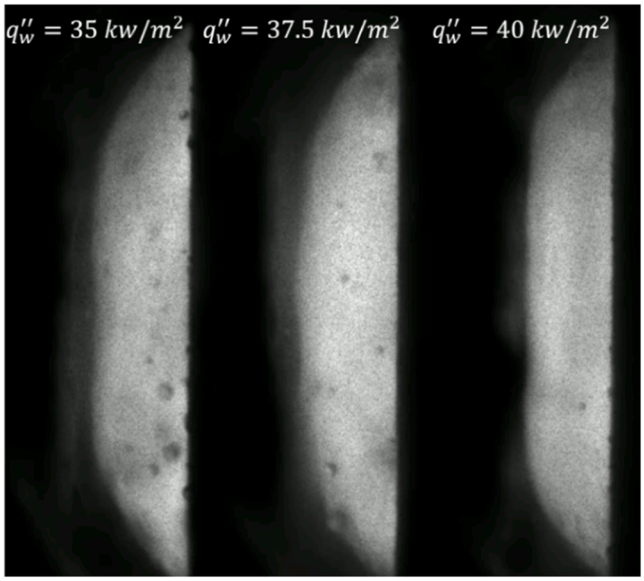

Fig. 6. Original image of the left side of the flow channel under increasing heat flux.

2.4. Uncertainties

In this paper, the target parameters from the experimental work is droplet size. For the further analysis of droplet size, the related parameters of operation conditions are mass flux, heat flux and pressure. The mass flux, heat flux and pressure are measured from measurement devices, which has certain measurement uncertainties. The droplet size is directly extract from images post-processing, which has certain uncertainties during the post processing. The parameters uncertainties are summarized in the Table 2.

Among them, the uncertainties occurred during the images post-processing are only be approximately estimated. The uncertainties in droplet size and position measurements are approximately ±0.01 mm, primarily due to pixel resolution limits and image binarization thresholds. It is also noted that droplets smaller than 0.04 mm cannot be reliably captured with the current optical setup. The resolution limit of droplet detection introduces a bias in the statistical analysis of cases with smaller droplets. To evaluate the uncertainty introduced by the 0.04 mm measurement threshold, a truncated gamma distribution fitting was applied to reconstruct the complete droplet size distribution, including the sub-threshold fraction. A gamma distribution was fitted to the measured data via maximum likelihood estimation and extrapolated below the cutoff to estimate the undetected droplets.

Fig. 7 and Fig. 8 illustrate the histogram of droplet size distribution and the fitted profiles of case 1 and case 9 in Table 1. The measured histograms (blue bars) represent the portion of measured droplets, while the fitted gamma distribution (red solid line) extends below the cutoff (orange dotted line), with the shaded red area indicating the estimated sub-threshold population. The difference between the experimental mean diameter ($d_{10,exp}$, blue dashed line) and the corrected mean of the fitted distribution ($d_{10,fit}$, red dashed line) quantifies the bias introduced by the threshold.

Table 2
Uncertainties.

Parameter	Mean Error
Pressure	0.14 %
Mass Flux	2.62 %
Heat Flux	2.41 %
Equilibrium steam quality	4.41 %
Droplet size	6.47 %

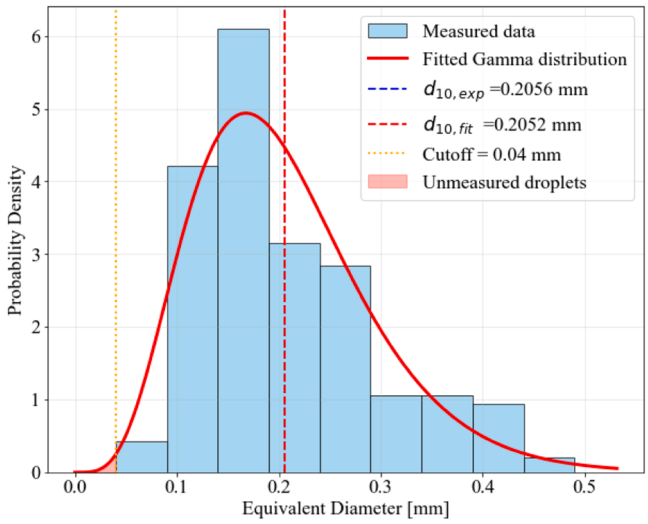

Fig. 7. Droplet size distribution and uncertainty analysis for low-pressure condition.

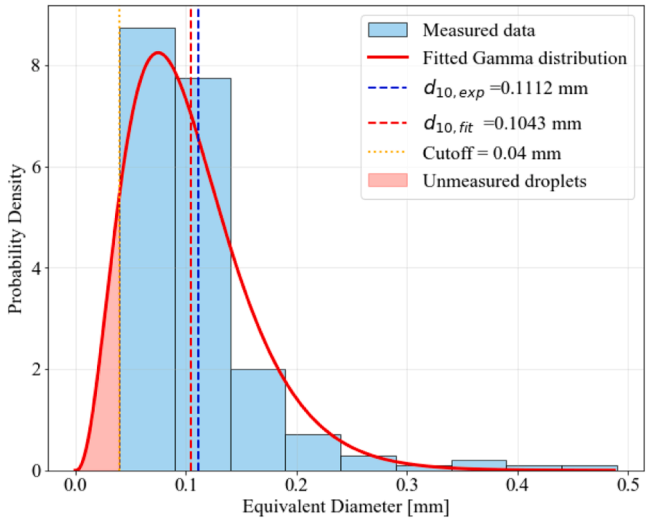

Fig. 8. Droplet size distribution and uncertainty analysis for high-pressure condition.

Fig. 7 displays the results at low pressure, the sub-threshold fraction is negligible, and the means are nearly identical ($d_{10,exp}$ = 0.2056 mm vs. $d_{10,fit}$ = 0.2052 mm). At high pressure, as shown Fig. 8, a relative higher portion of small droplets is undetected, resulting in a more noticeable discrepancy ($d_{10,exp}$= 0.1112 mm vs. $d_{10,fit}$ = 0.1043 mm). Quantitatively, the low-pressure case shows only 0.2 % of droplets below the cutoff, corresponding to a relative uncertainty of 0.18 % on average size, while the high-pressure case yields 8.5 % below the cutoff and a relative uncertainty of 6.68 %.

This analysis confirms that higher operating pressures promote smaller droplet formation and thus greater measurement uncertainty due to the limitation of current measurement methodology. Nevertheless, even under high reduced-pressure conditions, the maximum uncertainty remained below 7 %, demonstrating that the methodology ensures acceptable accuracy.

The experiments were repeated after approximately two months to check the reproducibility of the obtained data. In total, from the 31 PDO camera experiments, 10 cases of them were randomly selected and repeated. To assess the repeatability of the present experiments, both wall temperature and droplet size distributions were compared between original and repeated runs. Fig. 9 shows the wall temperature profile of Case 7 versus equilibrium quality for both measurements. The results exhibit very good repeatability, with deviations observed only near the dryout point, where the surface experiences periodic wetting and drying. In the stable PDO region, the profiles are nearly identical. For ten repeated cases, the wall temperature measurements yielded a mean error of 3.5 %, with maximum and minimum errors of 5.87 % and 0.83 %, respectively.

In addition, the droplet size distributions obtained from the original and repeated experiments of case 7 are showed in Fig. 10 and Fig. 11. From the distribution, they perform quite similar ranges and shapes. The average droplet size differed by only ~0.02 mm, which can be attributed to measurement uncertainty and minor variations in boundary conditions (e.g., heat flux and mass flux differences of <0.2 % and 1 kg/m²·s, respectively). These results confirm that the current experimental setup provides good repeatability for both wall temperature and droplet measurement.

3. Experimental results and analysis

3.1. Extracted droplet size from images

The case number 5 in Table 1, with pressure of 20.3 bar, mass flux of 150 kg/(m²·s), heat flux of 35 kW/m², is taken as an example to analysis the obtained droplet data in detail. Fig. 12 presents the histogram of droplet size distribution, illustrating the number of droplets corresponding to different size ranges. From the statistical analysis, it is observed that most droplets fall within the size range of 0.15 to 0.2 mm. The amount of droplets with larger or smaller sizes decreases. The minimum droplet size in this case is 0.06 mm, and the maximum recorded droplet size is 0.5 mm. Additionally, 90 % of the droplets fall within the range of 0.1 mm to 0.3 mm, among which 70 % are between 0.15 mm and 0.25 mm. In Fig. 12, it also shows the fitting of the droplet size distribution, indicating that the distribution follows both a gamma distribution and a lognormal distribution, which aligns well with previous experimental findings of Tatterson et al. [20], Ueda and Kim [24], and Cumo et al. [27] on droplet size distribution. This consistency confirms the reliability of data obtained in this study.

From the CFD simulations [7], it has been observed that the radial position of droplets significantly influences the droplet evaporation rate. Fig. 13 presents the radial distance of droplets from the wall, illustrating the number of droplets within each distance interval. It shows that the fewest droplets are found at the farthest distance from the wall. As the

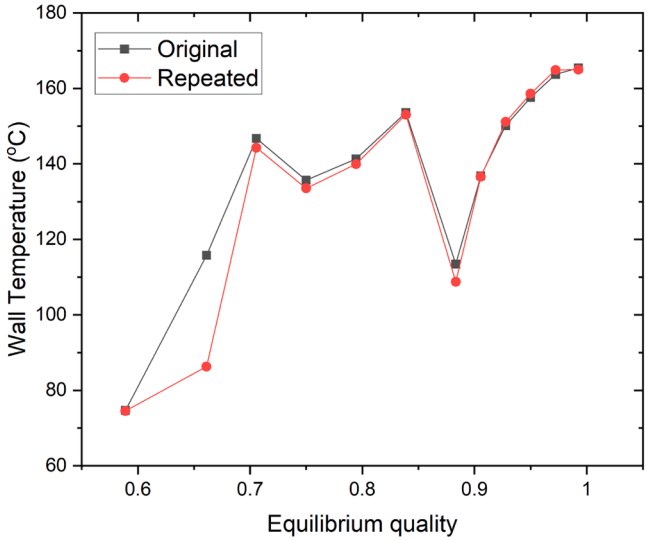

Fig. 9. Predicted wall temperature from original and repeated experiments.

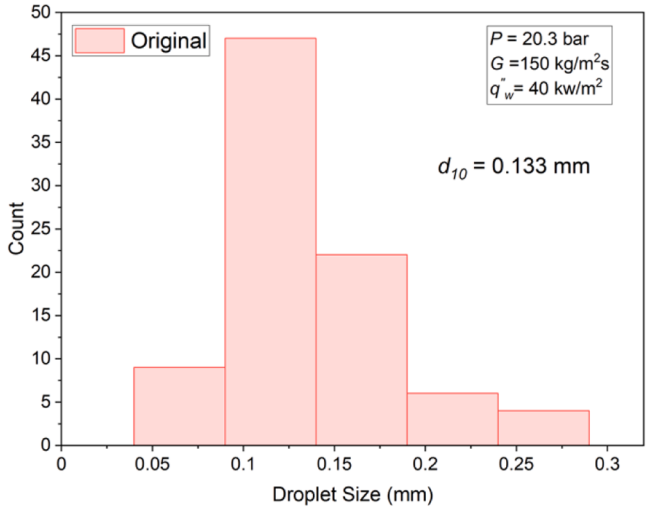

Fig. 10. Droplet size distribution of original experiment.

distance decreases, the droplet count gradually increases, reaching a peak. However, within 0.2 mm from the wall, the number of droplets drops sharply. This distribution closely resembles the droplet concentration profile obtained from CFD simulations [7,8]: due to lateral droplet transport, the droplet concentration increases progressively as droplets move closer to the wall. However, near the wall, intense evaporation caused by high vapor temperature leads to a decrease in droplet concentration.

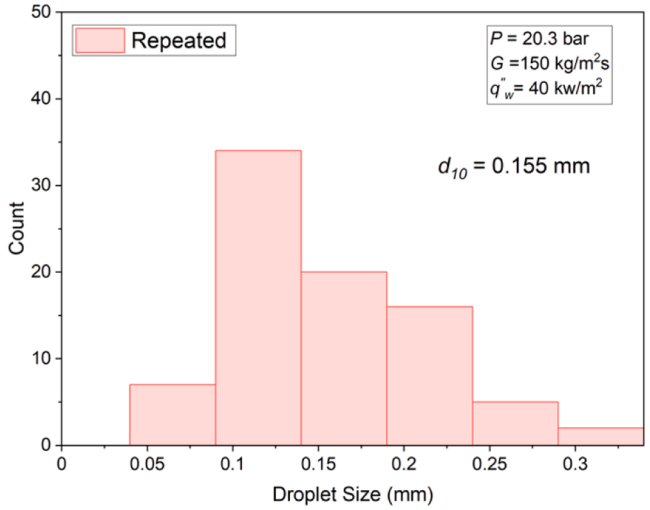

Fig. 11. Droplet size distribution of repeated experiment.

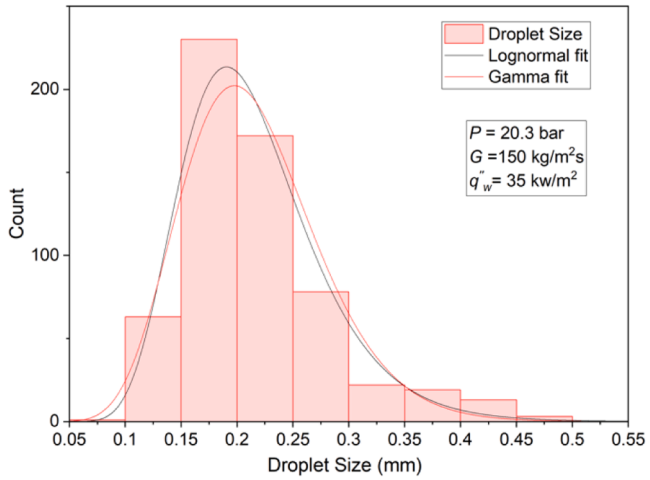

Fig. 12. Droplet size distribution with Lognormal and Gamma Fits.

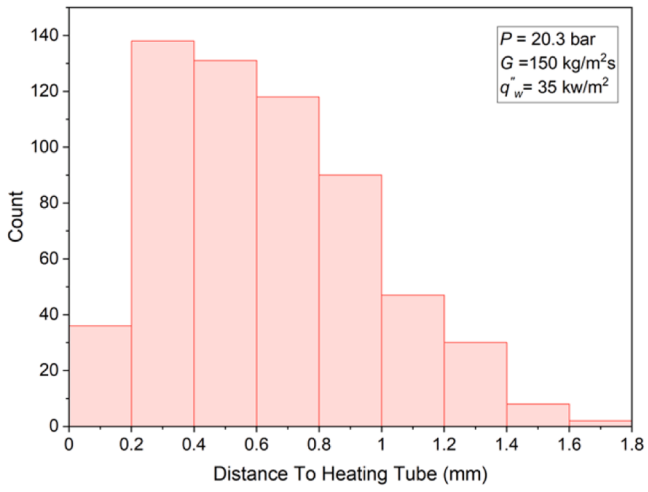

Fig. 13. Distribution of droplets' distance from the heating tube.

3.2. Analysis on droplet size

3.2.1. Statistical analysis

Fig. 14 presents the droplet size distribution under different heat flux conditions. It can be observed that as heating power increases, the overall distribution follows the same trend, shifting toward smaller sizes, indicating that more droplets become smaller while fewer droplets remain large. It can also be seen in the figure that as the heating power increases, the number of droplets that can be collected becomes less, which is consistent with the trend observed in Fig. 6. The significant reduction in the number of droplets is primarily attributed to the increase in local steam quality caused by higher heating power. Under the same pressure and mass flux conditions, a higher heat flux results in a larger amount of liquid being converted into vapor before reaching the observation window. Specifically, as the heat flux increases from 35 to 40 kW/m^2, the equilibrium steam quality at the observation location rises from 1.23 to 1.43. Consequently, a greater portion of the droplets evaporates all their mass upstream, leading to a marked decrease in the

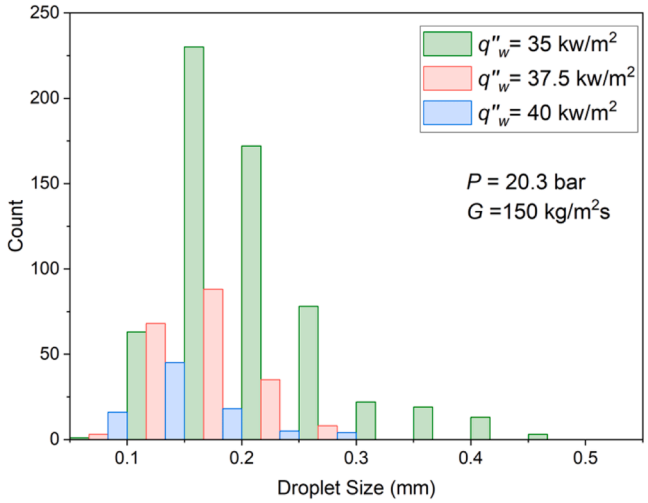

Fig. 14. Droplet size distribution under different heat fluxes.

number of droplets present in the observed region. Moreover, for relatively large droplets, the intensified heating over the same axial length promotes more evaporation, resulting in significantly smaller droplet sizes at the observation point.

Fig. 15 presents droplet size distributions at three different pressures, with reduced pressures P_R of 0.4, 0.5, and 0.8, respectively. The results indicate that as pressure increases, the droplet size distribution shifts to smaller values, and the most probable droplet size gradually decreases. This trend suggests that higher pressures lead to smaller droplet sizes, which could be attributed to the smaller surface tension of liquid at higher pressure. Additionally, at a low pressure of 0.4, the droplet size distribution follows well a gamma distribution. As the pressure increases, the peak and the curve gradually shift to the left, the left tail of the distribution curve gradually becomes invisible. At a higher pressure of 0.8, the most probable droplet size even falls within the minimum observable size range (0.04–0.09 mm). This is because this experiment cannot capture droplets smaller than 0.04 mm. The gamma distribution observed in other cases suggests possible presence of droplets smaller than 0.04 mm at higher pressures, which may have been missed due to measurement limitations. As a result, the proportion of uncounted droplets increases with pressure, indicating that actual droplet sizes at higher pressures are smaller than the measured values. This highlights the significant influence of pressure on droplet size in the PDO region.

Fig. 16 shows the histograms of droplet size distributions under different mass flux conditions. Cases with flow rates of 150 kg/(m^2·s) and 100 kg/(m^2·s) and relatively close equilibrium steam qualities of 1.33 and 1.26 are selected. It is evident that at higher mass flux, significantly more droplets are collected. While the overall size distribution and range remain similar for both mass flux conditions, the distribution at higher mass flux is noticeably steeper, with a sharper peak. This indicates that the proportion of small droplets is lower, and the droplet sizes are more concentrated around the most probable value. It can be attributed to the smaller wall temperature under higher mass flux, which is approximately 30 °C lower. This leads to smaller vapor superheating and thus lower evaporation efficiency, allowing droplets to retain slightly larger sizes. However, the increased vapor velocity at higher flow rates enhances aerodynamic shear, which limits droplet maximum size. As a result, the maximum droplet size under higher mass flux does not increase significantly, despite the reduced evaporation.

3.2.2. Average size analysis

After statistical analysis of the droplet size, the measured average droplet size d_{10}, which is also known as arithmetic mean droplet diameter, is obtained for further quantitative analysis.

Fig. 17 illustrates the variation in average droplet size for four cases

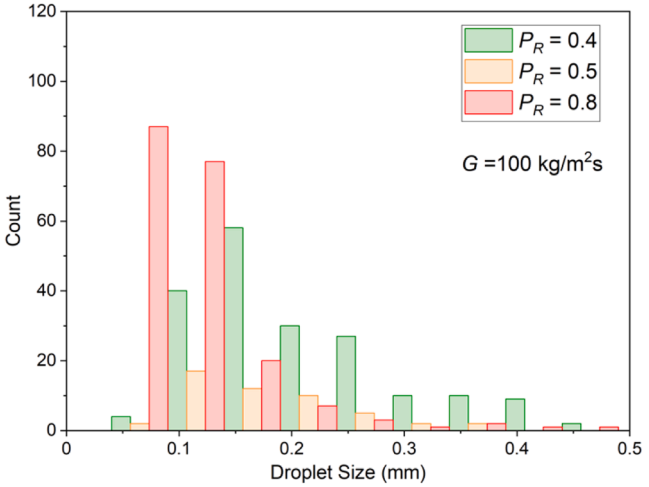

Fig. 15. Droplet size distribution under different pressures.

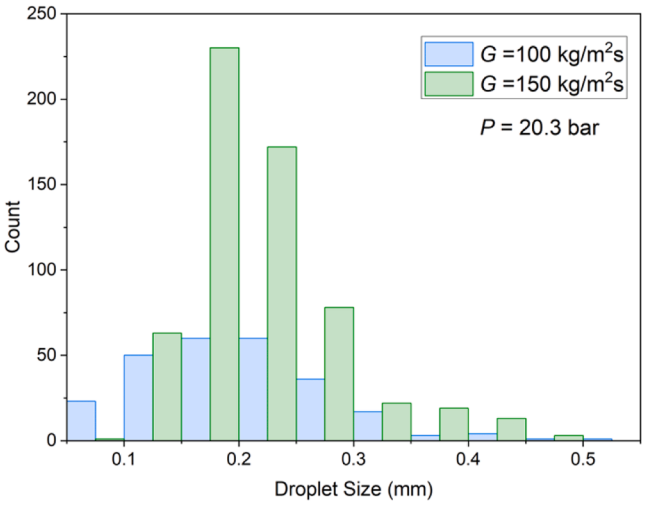

Fig. 16. Droplet size distribution under different mass fluxes.

with similar x_e and mass flux but different reduced pressures P_R. The black points represent experimental measured average droplet size, while the blue line provides a rough fitting curve to highlight the trend of the droplet size variation with pressure. The results indicate a clear trend: as pressure increases, droplet size decreases, with the reduction becoming more pronounced in the high-pressure region. A similar trend is also observed in Cumo's work. As shown in Fig. 18, the measured d_{10} from Cumo exhibits a relatively gradual decrease with increasing P_R in low pressure range. As P_R exceeds 0.7, the droplet size decreases at a significantly faster rate. The variation in droplet size with pressure can be analyzed based on the droplet formation and evaporation mechanism in dispersed flow. As pressure increases, substantial changes occur in fluid properties, including reduced surface tension, a smaller density difference between phases, and lower latent heat of vaporization. The reduction in surface tension tends to produce smaller droplets, whereas the decreased density difference between phases favors larger droplets. Additionally, lower latent heat enhances droplet evaporation, further reducing droplet size. A rough quantitative analysis of the combined effect of these properties revealed that the parameter governing the maximum droplet size, as determined by the critical Weber number, exhibits an approximately linear dependence on pressure, whereas the droplet size reduction due to evaporation, as described by Eq. (1), increases nonlinearly with pressure.

Thermal equilibrium steam quality x_e is a dimensionless parameter: under the same pressure, mass flux, and inlet temperature, a higher heat flux leads to a larger x_e. Therefore, the average droplet size is also

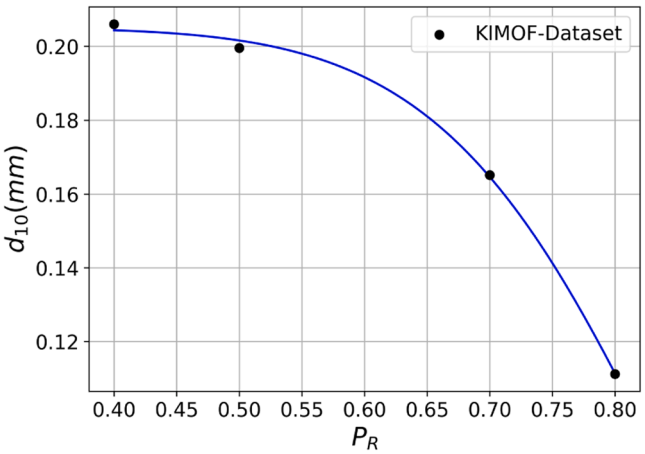

Fig. 17. Droplet mean size vs. reduced pressure in KIMOF experiment.

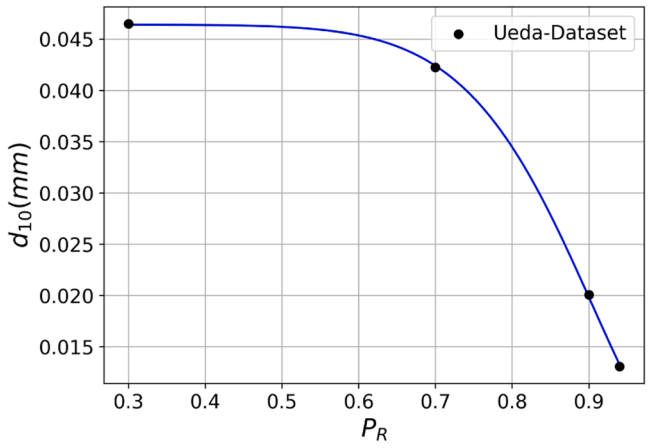

Fig. 18. Droplet mean size vs. reduced pressure in Cumo experiment.

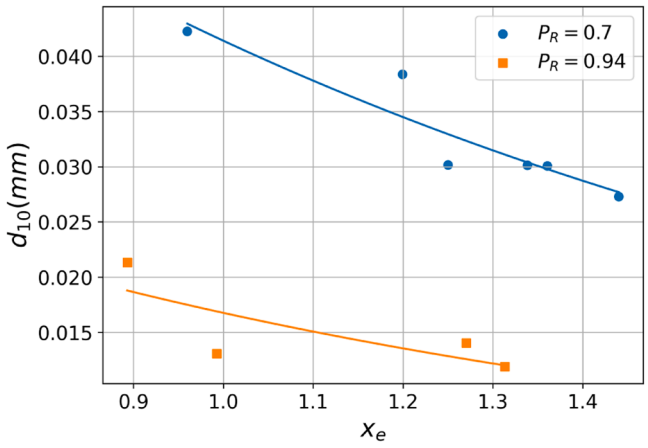

Fig. 20. Droplet mean size vs. Equilibrium steam quality at different pressures in Cumo experiment.

plotted against the thermal equilibrium steam quality, providing a dimensionless representation of the influence of heating on droplet size variation. As shown in Fig. 19, cases with different heat fluxes at a reduced pressure of 0.5 are presented. The blue and red lines depict the variation of d_{10} with x_e for mass fluxes of 100 kg/(m^2·s) and 150 kg/(m^2·s), respectively. The curves indicate a negative slop between droplet size and steam quality. As x_e increases, the average droplet size decreases due to the droplet evaporation in superheated vapor. This trend can be approximated by either a linear or an exponential fit.

On the other hand, it can be seen that under different mass fluxes, the decrease rate in droplet size as the increase of x_e is also different. At higher flow rates, the droplet size decreases more rapidly with increasing x_e. In region with smaller steam quality, the average droplet size is larger at higher flow rates, whereas in higher steam quality regions, the average droplet size is larger at lower flow rates.

Since Cumo et al. [27] operates experiments under constant mass flux, Fig. 20 plots their measured average droplet size and the corresponding x_e under different pressures and constant mass flux. It can be seen that the average droplet size decreases as the x_e increases, indicating a similar trend to that captured in current experiment work. These results also demonstrate the robustness and reliability of the current experimental approach.

4. Prediction of droplet size

Numerous empirical correlations have been proposed for predicting droplet size in PDO conditions, derived either from theoretical analyzes or experimental data fitting. In this subsection, the obtained droplet size data from current work are utilized to assess the reliability of these existing correlations. When discrepancies are identified, improvements are proposed to enhance the correlation's predictive capability.

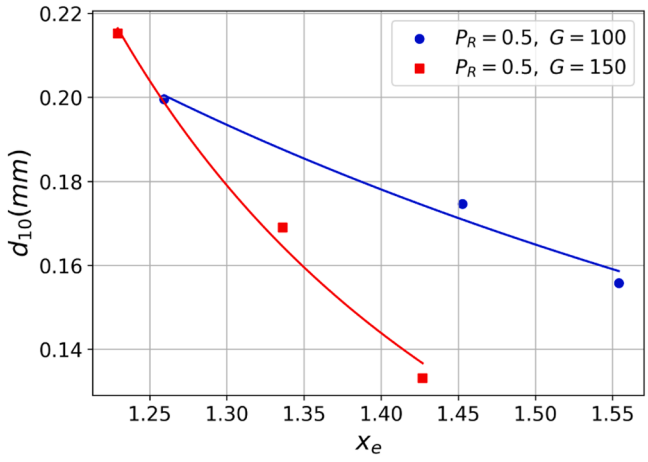

Fig. 19. Droplet mean size vs. Equilibrium steam quality at different pressures in KIMOF experiment.

4.1. Assessment of existing droplet size correlations

The average droplet size correlations of Kataoka et al. [23], Yoder and Rohsenow [4], Ueda and Kim [24], and Cumo et al. [27] are summarized in Table A1 in the Appendix and assessed in this section. (hereinafter referred to as Kataoka, Yoder, Ueda, Cumo).

4.1.1. Assessment with KIMOF experimental data

The correlations are firstly assessed with experiment data obtained from the present study, referred to as KIMOF below. Since the droplet size is obtained from the PDO region, the equilibrium steam quality x_e is used to calculate the vapor velocity in these applied correlations. The prediction results with the correlations from Cumo, Ueda and Kataoka are shown in Fig. 21(a), while Yoder's correlation which significantly deviates from the others, is displayed separately in Fig. 21(b). Among the evaluated models, Kataoka's correlation predicts the smallest droplet sizes, while Yoder's correlation significantly overestimates the average droplet size. The assessment results indicate that the Cumo and Ueda correlations demonstrate the best overall agreement with experimental data. However, discrepancies remain: Cumo's correlation underestimates droplet size at higher pressures, while Ueda's correlation, despite capturing the trend well, also tends to underestimate droplet size, necessitating further refinement.

4.1.2. Assessment with literature experimental datasets

Additional assessment is conducted using Cumo's experimental data. Cumo [27] conducted experiments using a visualized test section to measure droplet diameters under varying steam qualities and pressures, while maintaining a nearly constant mass flux of 900 kg/m^{2}s. The resulting correlation was developed using the most probable droplet size as the characteristic parameter to fit the experimental data. Consequently, when the average droplet size is extracted from Cumo's measurements, the predictions of Equation (A4) exhibits relatively larger deviations from the experimental values as shown in Appendix Fig. A1, particularly at intermediate and high pressures. This discrepancy is likely due to the inherent difference between the most probable droplet size employed in the correlation and the actual average droplet size observed in the experiments.

Additionally, the Ueda correlation tends to overestimate droplet size at higher pressures and underestimate it at lower pressures, suggesting that the pressure effect may not be fully captured in this correlation.

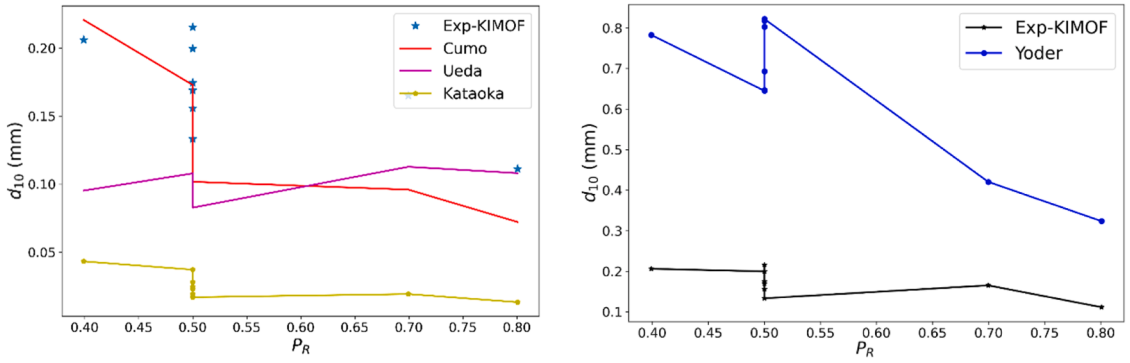

(a). Correlations of Cumo, Ueda and Kataoka

(b). Yoder correlation

Fig. 21. Assessment of literature droplet size correlations with the KIMOF data.

Furthermore, due to the absence of the heat flux data in Cumo's experiments, Yoder's correlation could not be evaluated under these conditions, as it explicitly relies on heat flux as an input parameter.

To further evaluate the predictive accuracy of these correlations, assessment is conducted using Ueda's dataset [24]. This dataset covers a wider mass flux range from 218 to 887 kg/m^{2}s, addressing the limited mass flux variations in the previous datasets and providing a broader basis for assessing the correlations across different mass flux conditions. As shown in the Appendix Fig. A2, Yoder's correlation significantly overpredicts the droplet size across all mass flux conditions. Cumo's correlation also exhibits a strong overestimation trend. Kataoka's correlation still underpredicts the droplet size. Among the evaluated models, only Ueda's correlation demonstrates good agreement with its own dataset, indicating that it captures the mass flux dependency more accurately than the others.

The assessments above reveal that Ueda's correlation shows the best performance., particularly when compared with Cumo's and Ueda's experimental data. However, it fails to capture the droplet size variation with pressure observed in the KIMOF experimental work. While Cumo's correlation provides good predictions for the present experiments, it significantly overpredicts droplet size when applied to Ueda's data. Yoder's correlation, on the other hand, consistently overpredicts all experimental data by a large margin. These findings highlight a key limitation: no single correlation accurately predicts droplet size under all conditions. Therefore, a new correlation need to be developed to improve overall predictive capability of droplet size.

4.2. Development of a new droplet size correlation

From Equation (A3) and (A4), Cumo's correlation is developed based on the droplet Reynold number (Re) while Ueda developed their correlation based on the ratio of droplet Weber number (We_d) and Re.

$$Re = \frac{(Gx_e)d_{10}}{\mu_l} \tag{3}$$

$$We_d = \frac{\rho_v u_v^2 d_{10}}{\sigma} \tag{4}$$

For droplets dispersed in the vapor flow, the density ratio influences the interfacial drag by affecting the slip ratio, while surface tension constrains the maximum droplet size. Therefore, to analyze the pressure effect on droplet size, the variations of surface tension and the vapor to droplet density ratio with pressure are examined in Fig. 22 and Fig. 23. The data points represent the trend of fluid property changing with reduced pressure P_R. As the pressure decreases, it can be seen that the density ratio between the phases increases, which indicates greater relative velocity between phases compared to conditions at higher pressure. Then the increased Weber number tends to reduce the maximum droplet size. However, simultaneously, the surface tension increases as pressure decreases, which would tend to increase the droplet size. Therefore, both surface tension and interfacial drag effects should be included to fully capture the pressure influence on droplet size.

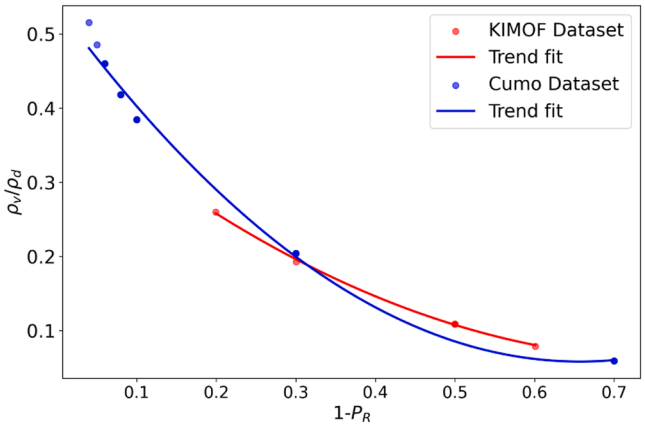

Fig. 22. Density Ratio vs. $(1 - \boldsymbol{P_R})$.

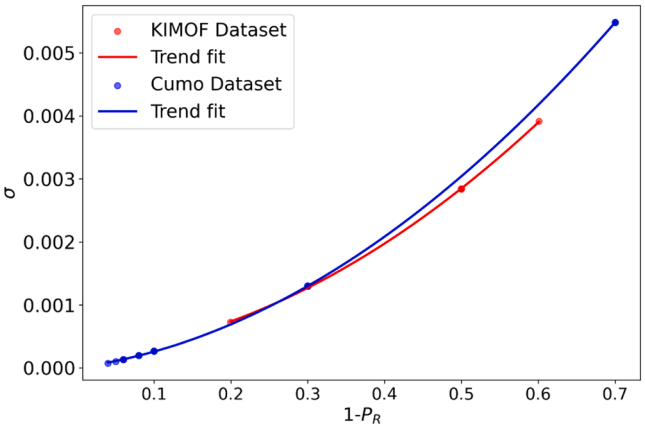

Fig. 23. Surface Tension vs. $(1 - \boldsymbol{P_R})$.

According to Cumo's work [27], the droplet Reynolds number exhibits a logarithmic and linear proportionality to the reduced pressure. However, as shown in the plot for the calculated droplet Reynolds

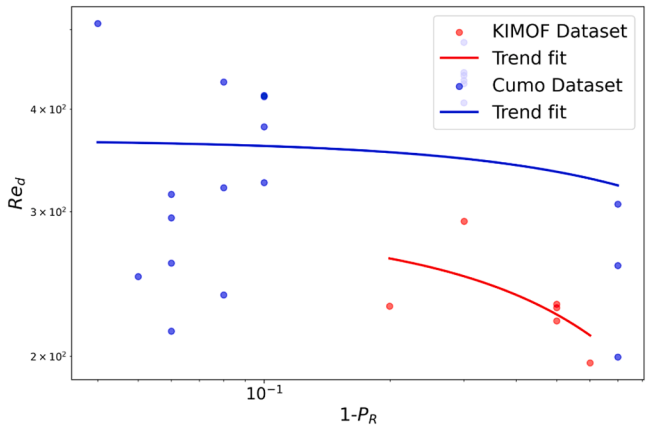

Fig. 24. Relationship of $\boldsymbol{Re}$ vs. $(1 - \boldsymbol{P_R})$.

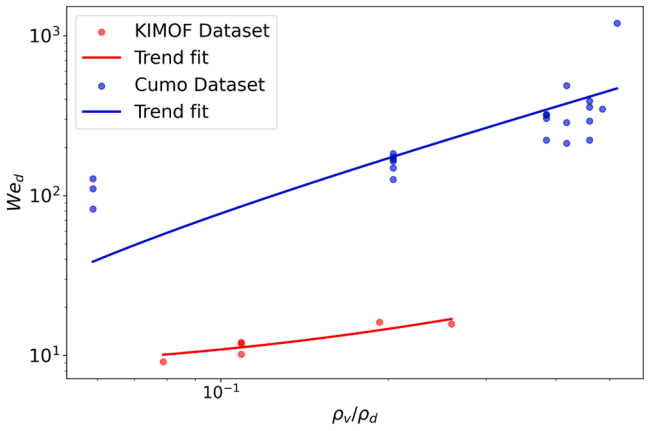

Fig. 26. Relationship of We_d vs. Density Ratio.

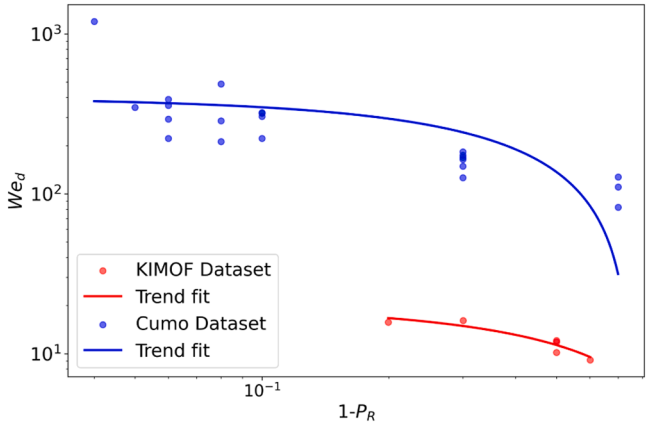

Fig. 25. Relationship of $\boldsymbol{We_d}$ vs.$(1 - \boldsymbol{P_R})$.

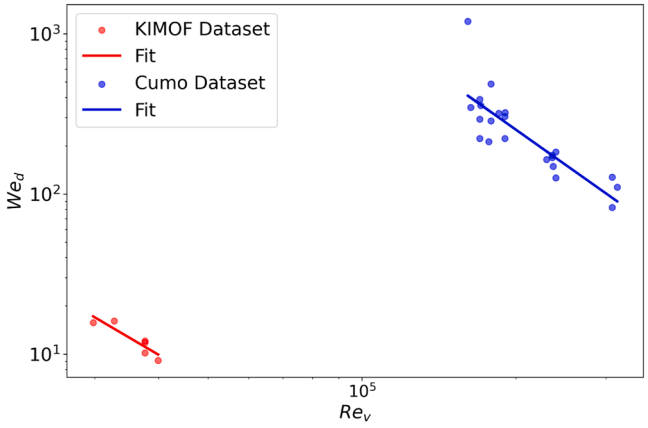

Fig. 27. Relationship of $\boldsymbol{Re_v}$ vs. $\boldsymbol{We_d}$.

number from experiment data of Cumo and KIMOF, displayed in Fig. 24, the relationship between droplet Reynolds number and $(1 - P_R)$ significantly deviates from linearity, especially the data from Cumo.

In Ueda's correlation as displayed in Equation (A 3), $\frac{\sigma}{\mu_g u_g}$ is the ratio of the droplet Weber number to the droplet Reynolds number. The tube diameter D_t on the left-hand side serves to non-dimensionalize the droplet size, implying a linear relationship between droplet size and tube diameter—an assumption that lacks clear physical justification. Given that surface tension is explicitly included (see Eq. (4)), the droplet Weber number is selected for analysis. In Fig. 25, the droplet Weber number are plotted against varying pressure and a well-fitted curve is observed. Therefore, the Weber number is adopted as the characteristic dimensionless parameter for developing an improved droplet size correlation in the present study.

To develop a correlation for the droplet Weber number, the relationships between various influencing parameters and the Weber number are systematically investigated. As discussed earlier, the effect of pressure on droplet size arises from the combined influence of surface tension and the gas-liquid density ratio. The surface tension component is inherently accounted for within the definition of the Weber number. The relationship between the Weber number and the density ratio is therefore analyzed and presented in Fig. 26. It is observed that the Weber number exhibits a clear positive and approximately linear correlation with the density ratio.

Besides, as shown in Fig. 27, the Weber number is log-linearly proportional to the vapor Reynold number Re_v, is calculated by $\frac{GD_t}{\mu_v}$. The vapor Reynolds number determines the flow regime and turbulence intensity within the tube, which in turn affects the shear environment and relative velocity between phases. Higher Re_v might lead to easier droplet breakup, reducing the droplet diameter, or, promoting droplet collisions. Therefore, the Re_v is also included to account for the effect from the vapor turbulence.

Therefore, using the experimental data from KIMOF and Cumo, nonlinear least-squares regression was performed with the default curve_fit function from the Python library scipy.optimize, which minimizes the sum of squared residuals. As a result, a correlation based on the droplet Weber number is correlated as the Eq. (5), relating the vapor Reynold number Re_v and density ratio ρ_v/ρ_d. As shown in Fig. 28, the predicted Weber number is plotted against the pressure $(1 - P_R)$ in dashed line and hollow points. By comparing with the Weber number calculated by experiment droplet size, the correlation in Eq. (5) accurately predicts the relationship between the Weber number and pressure across different mass flux conditions.

$$\frac{\rho_v u_v^2 d_{10}}{\sigma} = 3 \times 10^{-4} Re_v^{1.2} \left(\frac{\rho_v}{\rho_d}\right) \tag{5}$$

$$u_v = \frac{G x_e}{\rho_v} \tag{6}$$

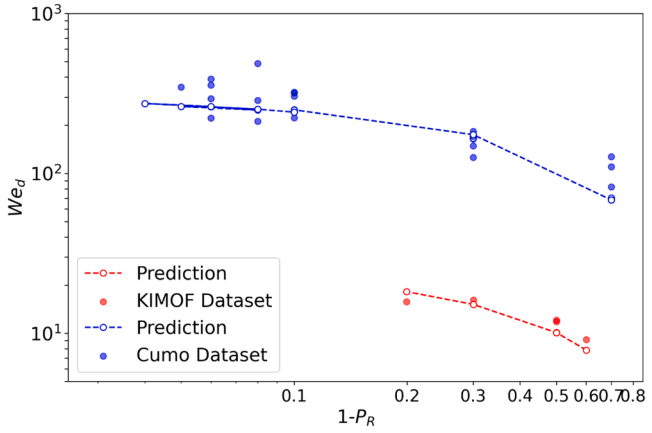

Fig. 28. Comparison of predicted and experimental $\boldsymbol{We_d}$ as the variation of $(1 - \mathbf{P_R})$.

$$Re_v = \frac{GD_t}{\mu_v} \tag{7}$$

Besides, based on Eq. (5), the average droplet sizes predicted by the newly developed correlation are presented in Fig. 29, together with the results from Ueda's and Cumo's empirical correlations. Fig. 29(a) shows the comparison between the predicted droplet sizes and the KIMOF experimental data, as a function of reduced pressure. It can be observed that the new developed correlation exhibits a better agreement with the experimental results and accurately captures the variation of droplet size with pressure, which is not well predicted by the Ueda and Cumo correlations. A similar trend is found in Fig. 29(b), where Cumo's experimental dataset is used for assessment. The newly developed correlation consistently outperforms the other two empirical models, particularly under high-pressure conditions, where it provides significantly more accurate predictions of droplet size.

Additionally, to further evaluate the generalizability of the new correlation, droplet size data from Ueda's experiments—which were not involved in the correlation development—are employed for validation. Fig. 30, presents the predicted droplet sizes as a function of mass flux, along with Ueda's measurements. It is evident that the new correlation maintains high predictive accuracy for these independent data, further confirming its robustness and applicability beyond the specific conditions used during its formulation.

The developed droplet size correlation demonstrates clear improvements in predictive accuracy compared with existing models. As summarized in Table 3, the mean error for the present datasets (KIMOF) is reduced to –11.84 % with an RMS error of 17.41 %, whereas the correlations of Cumo and Ueda yield substantially larger errors. Similarly, for Cumo's dataset, Eq. (5) decreases the mean error from –56.93 % (Cumo's correlation) to –13.54 %, and for Ueda's dataset, although the correlation of Ueda performs reasonably well, Eq. (5) still maintains acceptable predictive accuracy with a mean error of 29.50 % compared to extremely large deviations observed when using Cumo's correlation.

The good agreement of the new correlation with above three datasets demonstrates that the new droplet size correlation predicts the droplet size well under varying pressures and mass fluxes in PDO conditions.

The applicability of Eq. (5) has been established for Reynolds numbers between 30,000 and 720,000, reduced pressures of 0.3–0.97, and droplet Weber numbers from 10 to 1000. Within this range, the new correlation provides reliable predictions across three different fluids and a wide range of experimental conditions

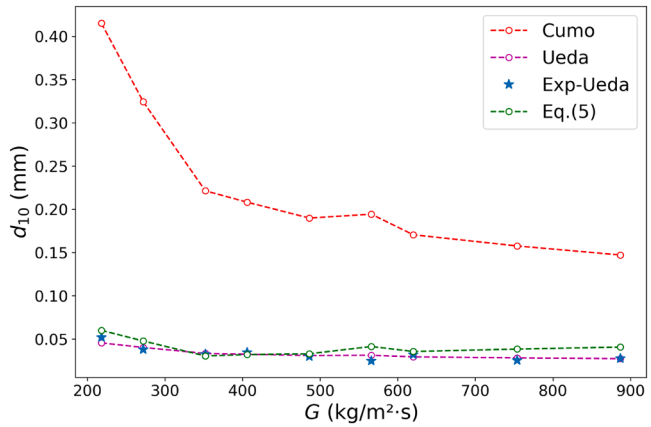

Fig. 30. Assessment of Eq. (5) with Ueda experiment data.

Table 3
Correlation error analysis.

Dataset	Correlation	Mean Error %	RMS Error %
KIMOF	Eq. (5)	−11.84	17.41
	Cumo_correlation	−23.56	28.66
	Ueda_correlation	−40.05	42.89
Cumo	Eq. (5)	−13.54	29.11
	Cumo_correlation	−56.93	60.46
	Ueda_correlation	27.04	44.67
Ueda	Eq. (5)	29.50	39.31
	Cumo_correlation	581.19	597.99
	Ueda_correlation	0.93	15.27

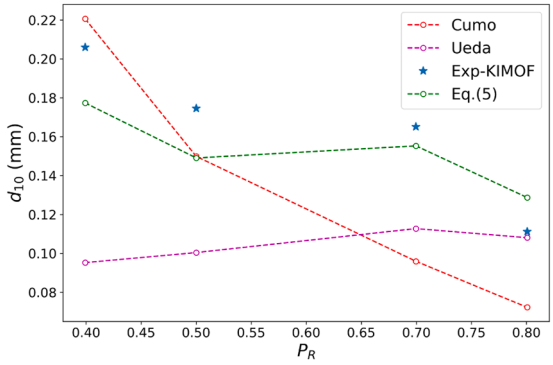

(a). Assessed with the KIMOF experiment data

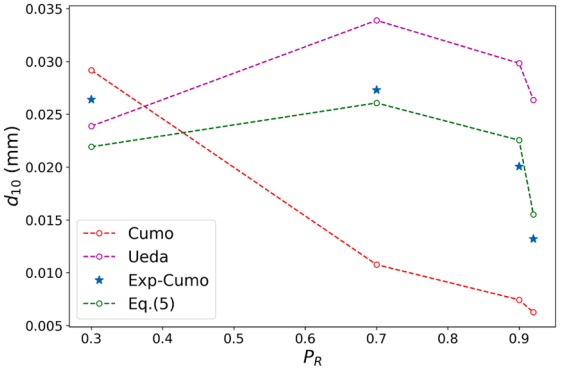

(b). Assessed with Cumo's experiment data

Fig. 29. Assessment of Eq. (5) and correlations from Cumo and Ueda.

Summary

This paper presents an experimental investigation on the droplet size in the PDO region. By post-processing the images, droplet size can be obtained under various conditions, including different pressures, mass fluxes and heat fluxes. Correlations of droplet size are assessed and improved using the experimental data from the present study and existing literatures. Key findings include:

- The droplet size distribution follows lognormal distribution and gamma distribution as the literature reported. Droplet size varies under different pressure, mass flux and heat flux. As heat flux increases, steam quality at the observation window also increases, resulting in a decrease in droplet size. A clear inverse relationship between steam quality and droplet size is observed by the comparison of the average droplet size with the equilibrium steam quality. Besides, an increase in pressure leads to a reduction in droplet size. The decrease rate of droplet size becomes more pronounced at high pressure ranges.
- Correlations from the literature are evaluated using the experimental data from the current study, as well as from the works of Cumo and Ueda. Among these, Yoder's model consistently overpredicts the droplet size, while Kataoka's model consistently underpredicts it. In contrast, Ueda's and Cumo's correlations provide more reasonable predictions. However, Cumo's correlation performs poorly when compared with Ueda's data, while Ueda's correlation fails to accurately predict the droplet size measured in the present study.
- A new correlation for the average droplet size under PDO conditions is developed.

$$\frac{\rho_v u_v^2 d_{10}}{\sigma} = 3\ \times 10^{-4} Re_v^{1.2} \left(\frac{\rho_v}{\rho_d}\right)$$

The inclusion of the droplet Weber number accounts for surface tension effects, while the interfacial drag effect, which varies with pressure, is incorporated using the density ratio. Additionally, the vapor Reynolds number is introduced to better capture turbulence effects on droplet size. Assessment with experimental droplet datasets demonstrates the high prediction accuracy of the new correlation.

Overall, the experimental results presented in this paper provide valuable insights into droplet dynamics in the PDO region. The effects of pressure, heat flux, and mass flux on droplet size are thoroughly investigated. The new developed correlation offers a more accurate prediction on droplet size, enhancing the overall understanding of droplet behavior in the PDO region.

Although the correlation has been developed and validated using three different fluids under a wide range of pressures (0.3–0.97) and mass fluxes (100–900 kg/m^{2}s), additional experimental data are still required to further validate and improve its robustness. In particular, tests at higher mass fluxes (above 1000 kg/m^{2}s) and with other fluids such as water would be valuable to extend the applicability of the correlation.

Author statement

We, the authors, confirm that this manuscript represents original work and has not been previously published or under consideration for publication elsewhere. All authors have approved the final version of the manuscript and agree with its submission to the journal.

We understand that the Corresponding Author is the sole contact for the Editorial process. She is responsible for communicating with the other authors about the progress, submissions of revision and final approval of proofs.

CRediT authorship contribution statement

Zihan Xia: Writing – original draft, Visualization, Validation, Software, Methodology, Investigation, Formal analysis, Data curation, Conceptualization. **Nikolai Rensch:** Writing – original draft, Investigation, Data curation. **Xu Cheng:** Writing – review & editing, Supervision, Resources, Project administration, Funding acquisition.

Declaration of competing interest

The authors declare that they have no known competing financial interests or personal relationships that could have appeared to influence the work reported in this paper.

Acknowledgements

This work is sponsored by the German Federal Ministry of Research, Technology and Space (BMFTR) under the contract number 02NUK062A. The partial financial support for the first author through China Scholarship Council (CSC) is highly appreciated. Responsibility for the content of this report lies with the authors.

Appendix

Table A1
Droplet size correlations from literature.

Author	Derived from	Droplet size correlation	
Kataoka [23]	Pre-dryout	$\frac{d_{10}}{D_t} = 0.0031 \frac{\sigma}{\rho_g u_g^2} Re_g^{\frac{2}{3}} \left(\frac{\rho_g}{\rho_l}\right)^{-\frac{1}{3}} \left(\frac{\mu_g}{\mu_l}\right)^{\frac{2}{3}}$	(A 1)
Yoder [4]	Dryout	$\frac{d_{10}}{D_t} = \frac{x_b - 0.1}{x_{do} - 0.1} \frac{d_{do}}{D_t} + \int_{x_b}^{x_{do}} \frac{d}{d_t} \frac{dx}{x_{do} - 0.1}$	(A 2)
Ueda [24]	Dryout	$\frac{d_{10}}{D_t} = 6.1\ \times 10^{-3} \left[\frac{\sigma}{\mu_g u_g} \times \left(\frac{\rho_g}{\rho_l}\right)^{1.25}\right]^{0.5}$	(A 3)
Cumo [27]	Post-dryout	$\frac{(Gx_e) d_{10}}{2\mu_l} = 123.1 * (1 - P_R)^{0.31}$	(A 4)

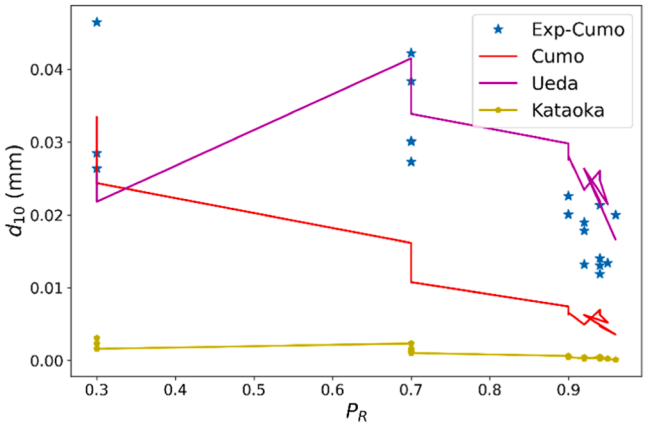

Fig. A1. Assessment of droplet size correlations with Cumo's experiment data.

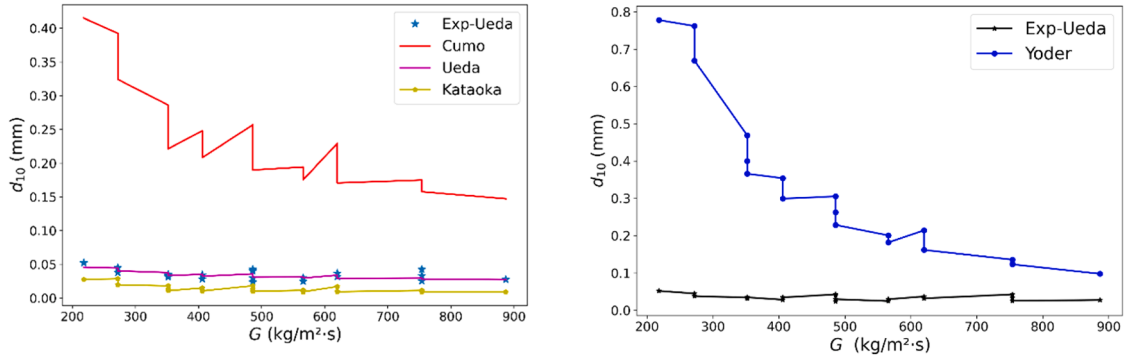

(a). Correlations of Cumo, Ueda and Kataoka (b). Yoder correlation

Fig. A2. Assessment of correlations with Ueda's experimental data.

Data availability

Data will be made available on request.

References

[1] N. Rensch, L. Köckert, A.F. Badea, X. Cheng, Experimental investigation of post-dryout heat transfer with R-134a at high pressures, Nucl. Sci. Eng. (2024) 1–20. October.

[2] M. Song, Modelling of CHF and post-CHF Heat Transfer For Trans-Critical Transients, Karlsruher Institut für Technologie (KIT), 2021. Ph.D. Thesis.

[3] Y. Guo, K. Mishima, A non-equilibrium mechanistic heat transfer model for post-dryout dispersed flow regime, Exp. Therm. Fluid sci. 26 (2002) 861–869.

[4] G. Yoder, W. Rohsenow, A solution for dispersed flow heat transfer using equilibrium fluid conditions, J. Heat Transf. 105 (1983) 10–17.

[5] J. Shi, B. Sun, G. Zhang, F. Song, L. Yang, Prediction of dryout and post-dryout wall temperature at different operating parameters for once-through steam generators, Int. J. Heat. Mass Transf. 103 (2016) 66–76.

[6] H. Li, H. Anglart, Prediction of dryout and post-dryout heat transfer using a two-phase CFD model, Int. J. Heat. Mass Transf. 99 (2016) 839–850.

[7] Z. Xia, X. Cheng, W. Liu, CFD simulation on droplet behavior in post-dryout region, Kerntechnik 89 (2024) 124–132.

[8] Z. Xia, X. Cheng, Numerical investigation on droplet lateral movement in post-dryout region, Int. J. Heat. Mass Transf. 237 (2025) 126448.

[9] N. Frossling, Uber die verdungtung fallenden Tropfen, Gerlands Beitr. Geophys. 52 (1938) 170–216.

[10] K. Lee, D. Ryley, The evaporation of water droplets in superheated steam, J. Heat Transf. 90 (1968) 445–451.

[11] X. Cheng, F. Feuerstein, D. Klingel, D.L. Yu, Mechanistic prediction of post dryout heat transfer and rewetting, Kerntechnik 83 (3) (2018) 203–207.

[12] T.F. Lin, J.F. Jou, C.H. Hwang, Turbulent forced convective heat transfer in two-phase evaporating droplet flow through a vertical pipe, Int. J. Multiph. Flow 15 (6) (1989) 997–1009.

[13] M. Andreani, G. Yadigaroglu, A 3-D eulerian–Lagrangian model of dispersed flow film boiling including a mechanistic description of the droplet spectrum evolution–I. The thermal-hydraulic model, Int. J. Heat. Mass Transf. 40 (8) (1997) 1753–1772.

[14] M.J. Meholic, The development of a non-equilibrium dispersed flow film boiling heat transfer modeling package, Ph.D. Thesis, The Pennsylvania State University, 2011.

[15] Z. Xia, X. Cheng, A new mechanistic model for post-dryout heat transfer based on two-region approach, Int. J. Heat. Mass Transf. 245 (2025) 127035.

[16] H.Y. Jeong, H.C. No, Modelling for post-dryout heat transfer and droplet sizes at low pressure and low flow conditions, Int. Commun. Heat Mass Transf. 23 (6) (1996) 767–778.

[17] D. Yu, Analysis and modelling of full-range post-dryout heat transfer in vertical tubes, Ph.D. Thesis, Karlsruher Institut für Technologie, 2019.

[18] A.F. Varone, The influence of the dispersed phase on the convective heat transfer in dispersed flow film boiling, Ph.D. Thesis, Massachusetts Institute of Technology, 1990.

[19] K. Matsuura, I. Kataoka, K. Mishima, Post-dryout heat transfer analysis model with droplet lagrangian simulation, JSME Int. J. B: Fluids Therm. Eng. 49 (2) (2006) 377–383.

[20] D.F. Tatterson, J.C. Dallman, T.J. Hanratty, Drop sizes in annular gas-liquid flows, AIChE J. 23 (1977) 68–76.

[21] J.C.B. Lopes, A.E. Dukler, Droplet sizes, dynamics and deposition in vertical annular flow, Houston Univ., TX (USA). Dept. of Chemical Engineering, NUREG/CR-4424, 1985.

[22] D.G. Evans, S.W. Webb, J.C. Chen, Measurements of axially varying non-equilibrium in post critical-heat-flux boiling in a vertical tube, Lehigh Univ., USA. Inst. of Thermo-Fluid Engineering and Science, NUREG/CR-3363, 1983.

[23] I. Kataoka, M. Ishii, K. und Mishima, Generation and size distribution of droplet in annular two-phase flow, J. Fluids. Eng. 105 (1983) 230–238.

[24] T. Ueda, K. Kim, Dryout heat flux and size of entrained drops in a flow boiling system, Bull. JSME 25 (1982) 225–233.
[25] T. Ueda, Entrainment rate and size of entrained droplets in annular two-phase flow, Bull. JSME 22 (1979) 1258–1265.
[26] R. Schnittger, Untersuchungen zum wärmeübergang bei vertikalen und horizontalen rohrströmungen im Post-dryout-Bereich, Ph.D. Thesis, TU-Hannover, 1982.
[27] M. Cumo, G. Farello, G. Ferrari, G. Palazzi, On two-phase highly dispersed flows, J. Heat Transf. 96 (1974) 496–503.
[28] B.J. Azzopardi, A. Piearcey, D.M. Jepson, Drop size measurements for annular two-phase flow in a 20 mm diameter vertical tube, Exp. Fluids 11 (1991) 191–197.
[29] Z. Wang, H. Liu, Z. Zhang, B. Sun, J. Zhang, W. Lou, Research on the effects of liquid viscosity on droplet size in vertical gas–liquid annular flows, Chem. Eng. Sci. 220 (2020) 115621.
[30] B. Bae, T. Kim, K. Kim, J.J. Jeong, B. Yun, Experimental investigation of droplet entrainment and deposition in horizontal stratified wavy flow, Int. J. Heat. Mass Transf. 144 (2019) 118613.
[31] L.B. Fore, B.B. Ibrahim, S.G. Beus, Visual measurements of droplet size in gas–liquid annular flow, Int. J. Multiph. Flow 28 (2002) 1895–1910.